Bulletin of the Seismological Society of America, Vol. 106, No. 4, pp. –, August 2016, doi: 10.1785/0120150298

Ⓔ

Distance and Azimuthal Dependence of Ground-Motion Variability for Unilateral Strike-Slip Ruptures

by Jagdish Chandra Vyas, Paul Martin Mai, and Martin Galis

Abstract We investigate near-field ground-motion variability by computing the seismic wavefield for five kinematic unilateral-rupture models of the 1992 M_w 7.3 Landers earthquake, eight simplified unilateral-rupture models based on the Landers event, and a large M_w 7.8 ShakeOut scenario. We include the geometrical fault complexity and consider different 1D velocity–density profiles for the Landers simulations and a 3D heterogeneous Earth structure for the ShakeOut scenario. For the Landers earthquake, the computed waveforms are validated using strong-motion recordings. We analyze the simulated ground-motion data set in terms of distance and azimuth dependence of peak ground velocity (PGV).

Our simulations reveal that intraevent ground-motion variability $\phi_{\ln(\mathrm{PGV})}$ is higher in close distances to the fault (<20 km) and decreases with increasing distance following a power law. This finding is in stark contrast to constant sigma-values used in empirical ground-motion prediction equations. The physical explanation of a large near-field $\phi_{\ln(\mathrm{PGV})}$ is the presence of strong directivity and rupture complexity. High values of $\phi_{\ln(\mathrm{PGV})}$ occur in the rupture-propagation direction, but small values occur in the direction perpendicular to it. We observe that the power-law decay of $\phi_{\ln(\mathrm{PGV})}$ is primarily controlled by slip heterogeneity. In addition, $\phi_{\ln(\mathrm{PGV})}$, as function of azimuth, is sensitive to variations in both rupture speed and slip heterogeneity. The azimuth dependence of the ground-motion mean $\mu_{\ln(\mathrm{PGV})}$ is well described by a Cauchy–Lorentz function that provides a novel empirical quantification to model the spatial dependency of ground motion.

Online Material: Figures of slip distributions, residuals to ground-motion prediction equations (GMPEs), distance and azimuthal dependence, and directivity predictor of ground-motion variability for different source models.

Introduction

Seismic-hazard analysis generally involves using ground-motion prediction equations (GMPEs), derived from strong-motion recordings, to estimate ground-shaking levels for future earthquakes. The GMPEs relate predictor variables Y such as peak ground velocity (PGV), peak ground acceleration (PGA), and pseudospectral acceleration (PSA) to explanatory variables such as earthquake magnitude, source-to-site distance, faulting style, and site class (e.g., Akkar and Bommer, 2007a,b; Abrahamson and Silva, 2008; Boore and Atkinson, 2008; Chiou and Youngs, 2008; Bindi *et al.*, 2014). Ground motions computed using GMPEs are given in terms of the natural logarithm of the median Y ($\mu_{\ln(Y)}$) and its standard deviation ($\phi_{\ln(Y)}$), typically referred to as ground-motion variability.

Ground-motion variability associated with ground-motion prediction results from incomplete data sets and imperfect modeling, that is, lack of knowledge (epistemic uncertainty) or uncertainty due to nature's randomness (aleatory variability). There are attempts to separate and quantify epistemic and aleatoric components of $\phi_{\ln(Y)}$ (Anderson and Brune, 1999; Atkinson, 2013), but here we assume that $\phi_{\ln(Y)}$ represents only aleatoric ground-motion variability (Boore and Atkinson, 2008; Campbell and Bozorgnia, 2008). $\phi_{\ln(Y)}$ can be further subdivided into an intraevent component (i.e., for a single event considering all records at the same source-to-site distance) and an interevent component (i.e., at a single receiver considering all events).

Strasser *et al.* (2009) summarized the problems and challenges when estimating $\phi_{\ln(Y)}$. Among these, the lack of near-field recordings in strong-motion data sets is perhaps the most important one. Also, the available data are biased: many recordings exist for a few earthquakes, whereas only a few strong-motion data were recorded for many events (in particular for earthquakes that occurred before 1994). It is

important to note that $\phi_{\ln(Y)}$ controls the shape of the seismic-hazard curve, in particular for long return periods, and thus has significant impact on probabilistic seismic-hazard analysis (e.g., Bommer and Abrahamson, 2006). Therefore, it is of paramount importance to understand and precisely quantify the sources of ground-motion variability to improve ground-motion prediction for future earthquakes.

GMPEs are commonly specified using constant $\phi_{\ln(Y)}$ (e.g., Boore *et al.*, 1997; Chiou and Youngs, 2006; Boore and Atkinson, 2008). Some of the more recent GMPEs have incorporated earthquake-magnitude dependence of $\phi_{\ln(Y)}$ (e.g., Abrahamson and Silva, 2008; Chiou and Youngs, 2008). $\phi_{\ln(Y)}$ has also been analyzed as a function of source-to-site distance and rupture style. The most recent GMPE of Boore *et al.* (2014) includes a distance dependence of $\phi_{\ln(Y)}$, which is constant up to a Joyner–Boore distance (R_{JB}) of 100 km, followed by a slight increase due to regional variations in anelastic attenuation. Investigating the Japanese KiK-net strong-motion catalog, Rodriguez-Marek *et al.* (2011) observed that $\phi_{\ln(Y)}$ not only depends on earthquake magnitude, but also on source-to-site distance. They also discovered that the correlation of $\phi_{\ln(Y)}$ with magnitude and distance is not consistent across different spectral periods. Imtiaz *et al.* (2015) found that the intraevent $\phi_{\ln(Y)}$ also shows distance dependence with rupture style: for bilateral ruptures, $\phi_{\ln(Y)}$ tends to increase with distance, whereas for unilateral ruptures, $\phi_{\ln(Y)}$ tends to decrease with distance. Youngs *et al.* (1995) reported that $\phi_{\ln(Y)}$ decreases with increasing magnitude and that the magnitude dependence is stronger for the interevent $\phi_{\ln(Y)}$ than for the intraevent $\phi_{\ln(Y)}$. In summary, ground-motion variability has been found to depend on earthquake magnitude, rupture style, distance, and azimuth. However, the corresponding number of studies is limited, whereas the governing physics of potential $\phi_{\ln(Y)}$ dependencies is not yet fully understood.

In general, ground motion and its variability are determined by source, path, and site effects (e.g., Mai, 2009). However, the lack of near-field recordings hampers the development of a complete understanding of the physical causes of ground-motion variability. Therefore, physics-based simulation techniques that include a specified but complex rupture processes and wave-propagation effects are used to compute and analyze near-field ground motion and its variability (e.g., Spudich and Frazer, 1984; Komatitsch and Tromp, 1999; Dumbser and Kaeser, 2006; Mai *et al.*, 2010). Ripperger *et al.* (2008) showed that the azimuthal dependence of interevent ground-motion variability is strongest in the backward-directivity region. Imperatori and Mai (2012) quantified how ground-motion variability is influenced by the level of heterogeneity in several earthquake source models, as well as by different 1D models of Earth structure. The source-induced ground-motion variability is important at short-to-intermediate periods (<2 s) but negligible at long periods, whereas ground-motion variability associated with crustal models becomes significant at intermediate-to-long periods (>0.5 s). Recently, Ramirez-Guzman *et al.* (2015) performed numerical simulations for the 1811–1812 New Madrid earthquakes, demonstrating that ground-motion variability is strongly affected by basin and rupture directivity effects. Mena and Mai (2011) employed kinematic rupture models to investigate the effect of source complexity on the near-field velocity pulses to quantify the directivity effect. They found that directivity pulses are primarily related to slip heterogeneity (i.e., the size and location of slip asperities).

In the present study, we perform numerical simulations to further investigate the influence of the earthquake rupture process on near-field ground-motion variability, addressing the directivity effects in particular. Henry and Das (2001) showed that both strike-slip and dip-slip earthquakes tend to be unilateral, as indicated by the average hypocenter location within 25% of the fault length from the nearest end of the fault. McGuire *et al.* (2002) found that approximately 80% of all large earthquakes ($M_w > 7$) are predominantly unilateral. Mai *et al.* (2005) investigated the location of hypocenter positions along-strike and down-dip directions from inverted earthquake source models for small-to-large earthquakes. They found that small earthquakes ($M_w < 6$) tend to rupture in the center of the fault plane, which can be due to the limited resolution of finite-source inversions for the small earthquakes. However, they observed that moderate-to-large earthquakes tend to nucleate towards one end of the fault, rupturing to the other end unilaterally (particularly strike-slip earthquakes). The unilateral character of large strike-slip earthquakes suggests that their near-field ground motions may contain a strong directivity effect. In such cases, the unilateral rupture propagation, combined with the *S*-wave radiation pattern, produces strong shaking in the region of the forward-rupture-propagation direction. We conjecture that this may lead to higher near-field ground-motion variability compared to bilateral ruptures. Therefore, we consider earthquakes with strong unilateral rupture propagation to investigate near-field ground-motion variability as a function of distance and azimuth. We attempt to gain a deeper physical understanding of ground-motion variability, but we do not provide any correction terms to existing GMPEs (e.g., Spudich and Chiou, 2008).

In our ground-motion simulations, we use kinematic rupture models in which the rupture process is specified by assigning the spatiotemporal evolution of slip on the fault in terms of local slip-velocity functions and the rupture velocity. The rupture models are chosen such that comparison with observations allows us to validate our simulations and develop a new $\phi_{\ln(Y)}$ parameterization that we then test against a large scenario event. We choose the 1992 M_w 7.3 Landers earthquake, which is characterized by unilateral rupture propagation with strong directivity effect (e.g., Somerville *et al.*, 1997). As the large scenario event, we use one of the M_w 7.8 ShakeOut unilateral ruptures on the San Andreas fault (Graves *et al.*, 2008). For both events, we simulate the seismic wavefield at a large number of sites and analyze corresponding PGV values. We restrict ourselves to PGV because the simulations would become prohibitively expensive for the higher frequencies needed to study PGA, which also would require

inclusion of seismic-scattering effects that may lead to decreasing directivity signature (e.g., Boatwright, 2007; Seekins and Boatwright, 2010; Imperatori and Mai, 2013). For our numerical simulations, we use a generalized finite-difference code based on a support operator method (SORD code by Ely *et al.*, 2008), which is second-order accurate in space and time and naturally handles geometrically complex kinematic source models embedded in 3D Earth structure.

The subsequent sections are organized as follows. First, we describe our approach to ground-motion simulations for the M_w 7.3 Landers earthquake and perform statistical analysis on the computed shaking levels. We then present our results on the observed spatial dependencies of $\phi_{\ln(Y)}$ and investigate the rupture parameters that control $\phi_{\ln(Y)}$ of low-frequency ground motions. Finally, we analyze the ground-motion simulations from a large M_w 7.8 ShakeOut scenario to validate our findings from the Landers earthquake.

Ground-Motion Simulations for the 1992 M_w 7.3 Landers Earthquake

In this section, we introduce the kinematic rupture models of the M_w 7.3 Landers earthquake and proposed 1D velocity–density structures, along with our source–receiver geometry to study ground-motion variability. We also statistically compare our synthetics with observed strong-motion data to validate our numerical simulations.

Kinematic Source Models

From the Earthquake Source Model Database (SRCMOD, Mai and Thingbaijam, 2014), we choose five published finite-fault kinematic rupture models inverted by five different research groups: (1) Cotton and Campillo (1995), (2) Hernandez *et al.* (1999), (3) Zeng and Anderson (2000), (4) Wald and Heaton (1994), and (5) Cohee and Beroza (1994). Subsequently, we refer to each of these rupture models by the name of the respective first author.

Table 1 lists certain inversion parameters used by these five groups: inversion method, type of data sets, frequency range, number of segments, and type of source time function.

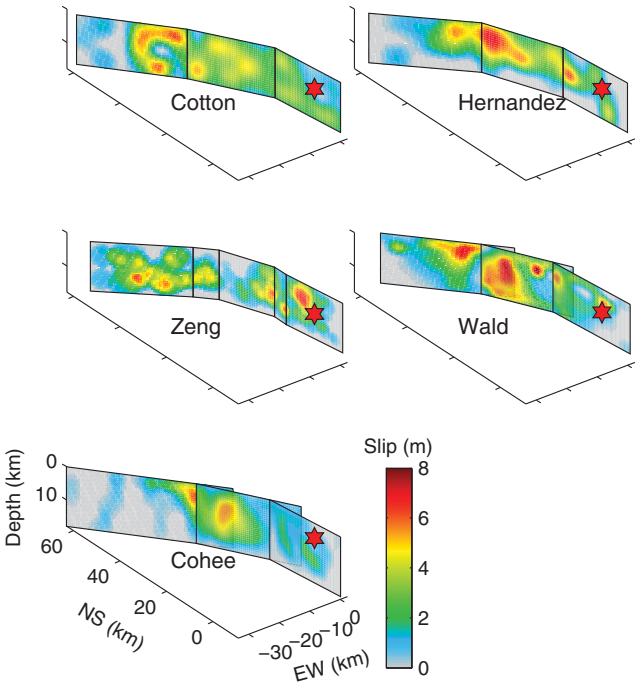

Figure 1. Bicubicly interpolated slip distributions of the five kinematic sources of the 1992 Landers earthquake used for the numerical modeling. Red stars denote the hypocenter location. Coordinates are given in east–west (EW) direction and north–south (NS) direction with respect to the epicenter as origin of a Cartesian coordinate system. Color-coded slip is in meters.

Figure 1 shows the bicubicly interpolated slip distributions of the five rupture models (the original slip distributions are displayed in Ⓔ Fig. S1, available in the electronic supplement to this article), illustrating variations in the assumed fault geometry among these models with respect to strike directions and overlapping or nonoverlapping segments. We interpolate the coarse inverted source models onto a finer grid to ensure a smooth seismic wavefield. The total seismic moment is conserved by rescaling interpolated slip values. The grid size of the inverted models varies between 0.5 and 5 km, whereas, for the interpolated sources, it ranges between 0.5 and 0.6 km.

Table 1
Source Parameters Used for Inversion by Five Different Groups

Parameter*	Cotton and Campillo (1995)	Hernandez *et al.* (1999)	Wald and Heaton (1994)	Cohee and Beroza (1994)	Zeng and Anderson (2000)
Frequency range (Hz)	0.05–0.5	0.05–0.5	0.077–0.5	0.05–0.25	0.13–1.43
Data sets	SGM	SGM, GPS, InSAR	SGM, Tele, GPS	SGM	SGM
STF	Tanh	Tanh	Triangular	Triangular	Composite
NTW	1	1	6	1	1
NSEG	3	3	3	3	5
Inversion method	Frequency domain inversion	Frequency domain inversion	Damped, linear least-squares inversion	Newton–Rephson iterative inversion	Genetic algorithm

SGM, strong ground motion; GPS, Global Positioning System; InSAR, Interferometric Synthetic Aperture Radar; and Tele, teleseismic.
*STF, source time function; NTW, number of time windows; NSEG, number of segments.

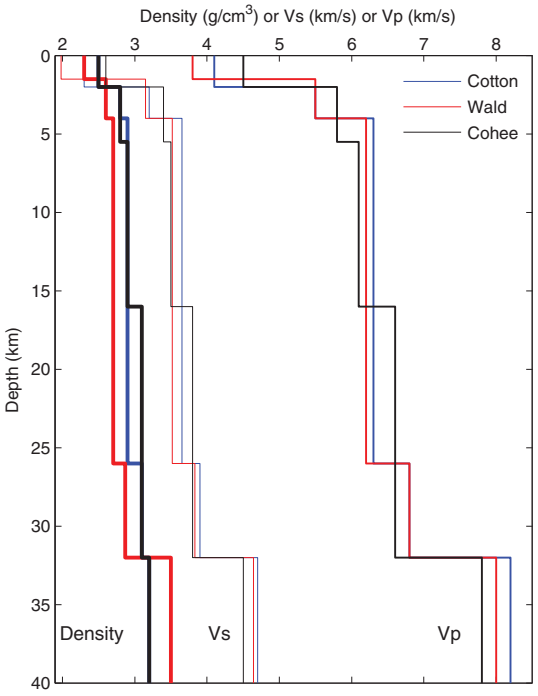

Figure 2. 1D velocity–density models used for the ground-motion simulations of the 1992 Landers earthquake.

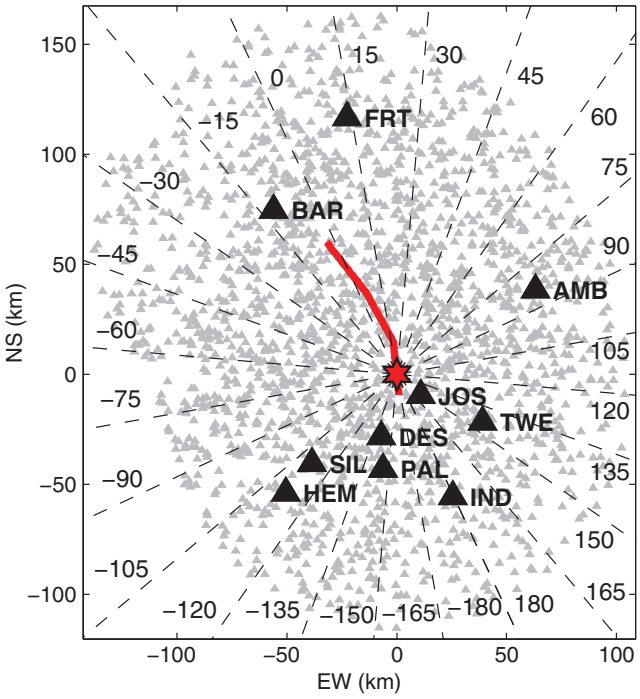

Figure 3. Source–receiver geometry in a Cartesian coordinate system centered on the epicenter. The red line represents the surface projection of the fault geometry for the Cotton and Campillo (1995) source model. The black triangles depict 10 California Strong Motion Instrumentation Program (CSMIP) strong-motion stations used to validate the simulations. The gray triangles show receivers used in the ground-motion variability investigation. The dashed black lines mark azimuthal directions with respect to average strike (335°) and origin as epicenter.

Earth Structure and Attenuation

For our ground-motion simulations, we apply the same 1D-layered Earth models as used in the corresponding inversion studies for the Cotton, Hernandez, Wald, and Cohee source models. For the Zeng source model, we adopt the medium parameters of Wald and Heaton (1994). Figure 2 displays the corresponding depth distributions of seismic-wave speeds and density.

Because intrinsic attenuation is not implemented in the SORD code, we apply a Futterman filter based on the t^*-operator that depends on travel time and Q-values (Varela *et al.*, 1993). The Cotton, Hernandez, and Wald models have been inverted considering depth-dependent Q. We obtain a representative Q-value by calculating the weighted harmonic mean of Q for the three models, with weights assigned according to layer thicknesses. The representative Q-values for Zeng and Cohee models are adopted from the Wald model. The average Q-values then range from 216 to 481, depending on the Earth structures used by different groups.

Receiver Configuration

To validate our simulations, we use recordings from 10 stations of the California Strong Motion Instrumentation Program (CSMIP) (Fig. 3, black triangles), obtained from the Consortium of Organizations for Strong Motion Observation Systems (COSMOS) website (see Data and Resources). For detailed statistical analysis, we consider a set of 2500 receivers, randomly distributed to avoid any potential spatial bias (Fig. 3, gray triangles). The station coordinates are fixed with respect to the corresponding epicenter and are identical for all considered rupture models. To avoid numerical artifacts due to inaccurate point-source representation at very small source–receiver distances, we do not include any station with R_{JB} less than 1 km. Therefore, the receivers used for our statistical analysis of ground-motion variability occupy the R_{JB} range from 1 to 106 km (Fig. 3).

Synthetic Seismograms and Validation

We restrict the maximum frequency in our simulations to 0.5 Hz, consistent with the frequency range for which the kinematic models have been obtained (Table 1). Because the SORD code is second-order accurate in space and time, we parameterize the simulations with a minimum of 15 points per shortest wavelength to achieve accurate wave propagation, leading to spatial grid sizes between 250 and 300 m (depending on the corresponding velocity model). The computational time step satisfies the numerical stability criteria given by Ely *et al.* (2008) and ranges from 0.015 to 0.020 s, depending on the particular velocity model.

For validation, we compare residuals of peak ground displacement (PGD) between our simulations and strong-motion observations, computed as $\text{res} = \ln(\text{PGD}_{\text{obs}}/\text{PGD}_{\text{sim}})$ (Fig. 4a). All seismograms are band-pass filtered in the

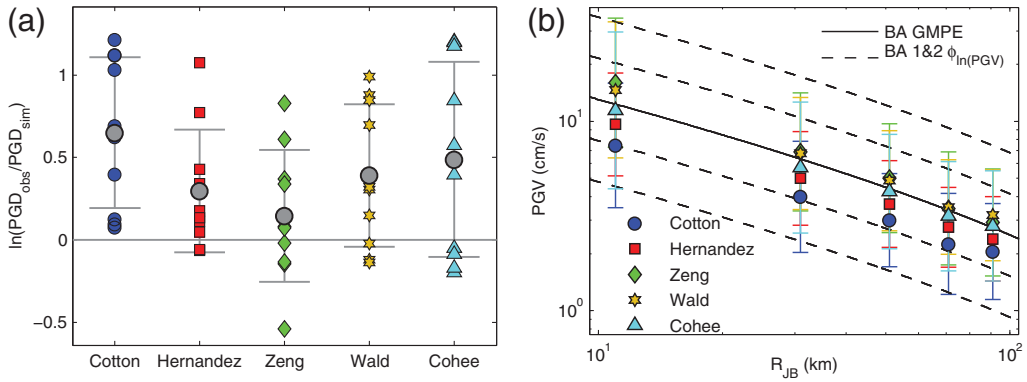

Figure 4. (a) Statistical summary of peak ground displacement (PGD) residuals (in natural-log scale) between simulated and observed waveforms for the five source models of the Landers earthquake. Different markers are used for different source models. The gray circles show the calculated mean residual, and gray bars show standard deviation for every source model. (b) Comparing mean and standard deviation of peak ground velocity (PGV) computed from simulations with a ground motion prediction equation (GMPE) (Boore and Atkinson, 2008). Different colored markers represent means of PGVs, and the bar indicates the corresponding standard deviation.

0.05–0.5 Hz frequency range using a second-order Butterworth filter. We determine PGD using the sensor-orientation independent measure GMRotD50 (Boore *et al.*, 2006), calculated by rotating the two orthogonal horizontal components from 1° to 90° in steps of 1° and computing the geometric mean for each pair. The final PGD value is then given as the median of 90 geometric means. We also calculate the residual mean and standard deviation for the 10 stations and for each model (Fig. 4a), noting that most stations are located in the backward-rupture-propagation direction. We find that our simulations slightly underestimate PGD values, although the zero-residual line falls within the one standard deviation for all but the Cotton model. We note that the Zeng model yields the lowest residuals, which we attribute to the fact that the Zeng model was inverted using seismic data up to 1.4 Hz, whereas the remaining models use seismic waves only up to 0.5 Hz, or even 0.25 Hz (Cohee model). Because our main target is investigating the spatial variability of ground motions in a relative sense, but not in absolute amplitude, we consider the level of agreement between synthetic and recorded wavefield as satisfactory.

In addition, we compare our simulations with a chosen GMPE by computing PGV from synthetic seismograms at 2500 sites, again using the sensor-orientation independent measure GMRotD50. We then bin the PGV values with respect to R_{JB} (bin width = 20 km) and compute the natural-log-normal mean $\mu_{\ln(PGV)}$ and standard deviation $\phi_{\ln(PGV)}$ for each bin. The bin width is chosen such that each bin contains at least 200 samples, whereas the mean R_{JB} of all stations within any bin is near the center of the bin. We find that the simulation-based estimates of PGV fall within the two intraevent standard deviations of the selected GMPE (Boore and Atkinson, 2008) (Fig. 4b).

The above steps of validating our ground-motion simulation approach ensure that our subsequent analysis of ground-motion variability will not suffer from numerical artifacts or any unrealistic assumptions or parameter choices.

Analysis of Ground-Motion Variability

In this section, we analyze the ground-motion variability of PGV with respect to R_{JB} and the source-to-site azimuth and compare PSA values from our simulations with GMPE-derived PSA estimates. We also consider an approach to correct ground-motion amplitudes with respect to directivity due to the rupture-propagation directionality (Spudich and Chiou, 2008).

Distance Dependence

For the analysis of ground-motion variability, we bin the PGV values at 2500 sites with respect to R_{JB} distance using a bin width of 20 km, with the constraint that each bin has at least 200 stations. We also test the effect of bin width on $\phi_{\ln(PGV)}$ by considering smaller (15 km) and larger (25 km) bin widths and find that all considered bin widths lead to similar results (compare Fig. 5 with Ⓔ Fig. S2a,b).

Figure 5 shows the distance dependence of the mean ($\mu_{\ln(PGV)}$) and the standard deviation ($\phi_{\ln(PGV)}$) of ln(PGV). As expected, $\mu_{\ln(PGV)}$ decreases with increasing distance for all five models due to geometrical spreading and attenuation. For reference, we also display the intraevent ground-motion variability from four GMPEs (Abrahamson and Silva, 2008; Boore and Atkinson, 2008; Campbell and Bozorgnia, 2008; Chiou and Youngs, 2008). We observe that $\phi_{\ln(PGV)}$ from our simulations is higher in the very-near-field region ($R_{JB} < 20$ km) than that estimated by GMPEs, but $\phi_{\ln(PGV)}$ decreases with increasing distance approaching the constant values of the GMPEs.

To examine the distance dependence of ground-motion variability, we model the $\phi_{\ln(PGV)}$ dependence on R_{JB} as a power law, $\phi_{\ln(PGV)} = \alpha R_{JB}^{k}$. We estimate the values of the parameters α and k using least-square fitting (Table 2; corresponding curves are shown by dashed lines in Fig. 5). We also calculate the mean value of $\phi_{\ln(PGV)}$ and the power-

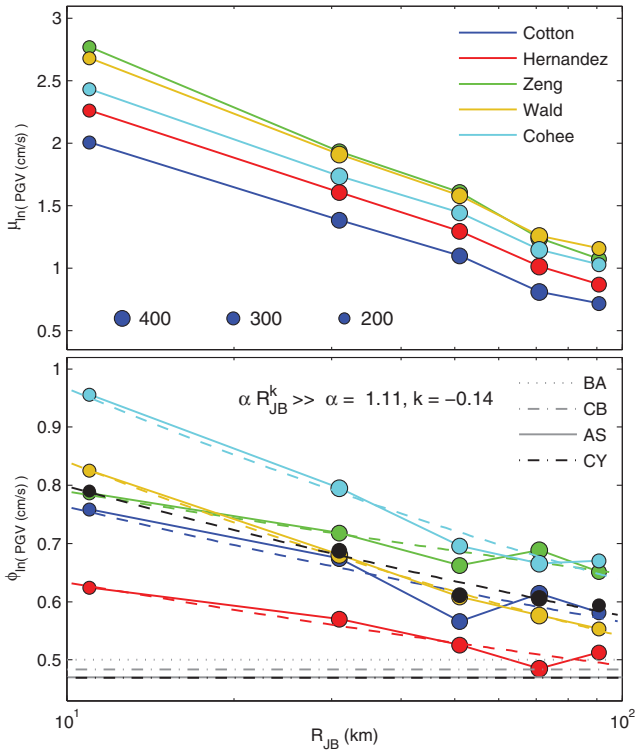

Figure 5. Distance dependence of the mean ($\mu_{\ln(PGV)}$) and the standard deviation ($\phi_{\ln(PGV)}$) of ln(PGV) for the five source models of the Landers earthquake (bin width = 20 km). The circle size indicates the number of stations in each bin. The black circles are the average $\phi_{\ln(PGV)}$. $\phi_{\ln(PGV)}$ decreases as a power law (αR_{JB}^{k}) with increasing distance. The dashed line shows the least-squares fit to the corresponding $\phi_{\ln(PGV)}$ values for different source models. Abbreviations are as follows: BA, Boore and Atkinson (2008); CB, Campbell and Bozorgnia (2008); AS, Abrahamson and Silva (2008); and CY, Chiou and Youngs (2008).

law fit for the ensemble (depicted by black circles and dashed lines in Fig. 5). We find $\alpha = 1.11$ and $k = -0.14$ for the mean $\phi_{\ln(PGV)}$. For all cases considered, α is always positive, ranging between 0.82 and 1.47, whereas k is always negative, ranging from −0.19 to −0.09. We find that the approximation by a power law is applicable over the entire R_{JB} range considered in this study ($1 < R_{JB} < 106$ km), but we cannot assess whether this trend persists to larger distances.

The space–time complexity of the earthquake rupture process has significant influence on near-field ground motion and its variability. In particular the directivity effect, due to a combination of the rupture-propagation direction and the S-wave radiation pattern, generates vastly different ground-motion amplitudes in the near field of large earthquakes, depending on whether the rupture propagates towards (forward directivity) or away (backward directivity) from a site. The Landers earthquake had strong directivity effect, as first identified by Somerville *et al.* (1997), resulting in higher ground motion in the northern part of the fault because of the unidirectional (south-to-north) rupture propagation. The effect of geometrical spreading is the same for all sites

Table 2
Parameters α and k of the Power Law (αR_{JB}^{k}) Obtained by Least-Squares Fitting to the Distance Dependence of $\phi_{\ln(PGV)}$ for the 1992 Landers Earthquake

Source Name	α	k
Cotton and Campillo (1995)	1.03	−0.13
Hernandez *et al.* (1999)	0.82	−0.11
Zeng and Anderson (2000)	0.96	−0.09
Wald and Heaton (1994)	1.31	−0.19
Cohee and Beroza (1994)	1.47	−0.18
Average $\phi_{\ln(PGV)}$*	1.11	−0.14

*PGV, peak ground velocity.

at a particular R_{JB} distance and therefore does not affect the $\phi_{\ln(PGV)}$ value for specific R_{JB} distance. Consequently, geometrical spreading is not the cause for the distance decay of $\phi_{\ln(PGV)}$, although it contributes to the distance decay of $\mu_{\ln(PGV)}$. On the other hand, the directivity effect is strong at near-source distances and becomes weaker farther away from the source. Therefore, we interpret the distance decay of $\phi_{\ln(PGV)}$ as a consequence of the strong directivity effect. The power-law exponent k will be large (or small) in the presence of strong (or weak) directivity. When the exponent k is zero, $\phi_{\ln(PGV)}$ is equal to α (i.e., $\phi_{\ln(PGV)}$ becomes constant), consistent with ground-motion variability of standard GMPEs.

The five Landers source models considered here are derived by inversion of seismic and/or geodetic data. Ideally, they should predict identical ground motions. However, the uncertainties in kinematic inversions manifest themselves in intraevent ground-motion variability of the estimated rupture parameters, which consequently contribute to predicted ground motion and their variability (Fig. 5). Our results show that the uncertainty of the inverted source models does not change the power-law decay trend of $\phi_{\ln(PGV)}$; however, it does affect the absolute values of $\phi_{\ln(PGV)}$.

Azimuthal Dependence

Next, we analyze ground-motion variability as a function of azimuth. Because the five rupture models have complex fault geometry, we compute azimuth with respect to the average strike direction and epicenter of each model. The azimuth values range from 0° to 180° and from 0° to −180°, measured in clockwise and anticlockwise directions, respectively. The PGV values at the 2500 sites are then binned with respect to azimuth to compute the mean ($\mu_{\ln(PGV)}$) and the standard deviation ($\phi_{\ln(PGV)}$) of PGV, considering a lognormal distribution. We choose a bin width of 15° to ensure that each bin has at least 30 stations, and we require that the mean azimuth lies near the center of the bin. To verify that our analysis does not depend on the bin width, we calculate $\mu_{\ln(PGV)}$ and $\phi_{\ln(PGV)}$ also for bin width 30° (compare Fig. 6 with Ⓔ Fig. S3).

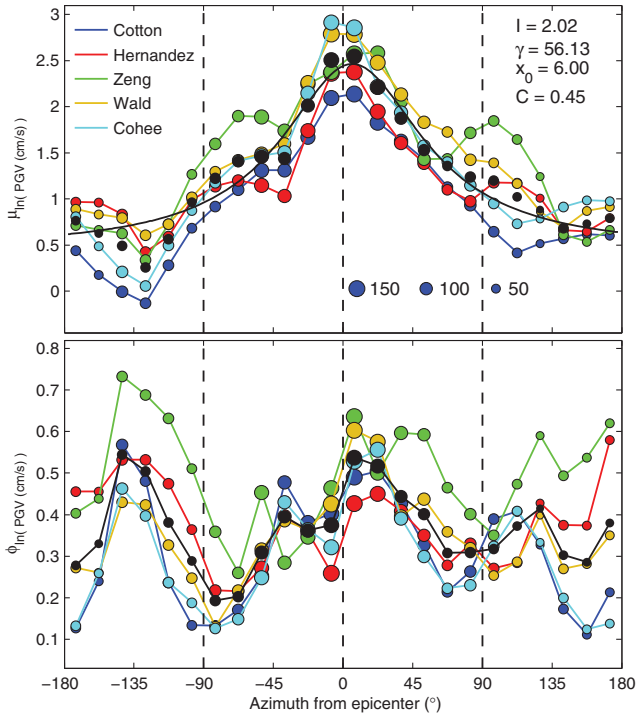

Figure 6. Azimuthal dependence of $\mu_{\ln(\mathrm{PGV})}$ and $\phi_{\ln(\mathrm{PGV})}$ for the five source models (bin width = 15°). The circle size represents the number of stations in each bin. The black circles and line marks the average $\mu_{\ln(\mathrm{PGV})}$ and average $\phi_{\ln(\mathrm{PGV})}$ for the five source models. The coefficients I, γ, x_0, and C of the Lorentz function (black line) are obtained from nonlinear optimization for average $\mu_{\ln(\mathrm{PGV})}$; 0° azimuth represents the average strike direction.

Figure 6 shows the azimuthal dependence of $\mu_{\ln(\mathrm{PGV})}$ and $\phi_{\ln(\mathrm{PGV})}$. As expected, $\mu_{\ln(\mathrm{PGV})}$ is highest in the forward-directivity region (i.e., for average strike direction with azimuth 0°) and lowest in the backward-directivity region (i.e., for azimuth ±180°). This pattern reflects strong directivity effects. We compute average $\mu_{\ln(\mathrm{PGV})}$ and find that it is well described by a Cauchy–Lorentz function (Fig. 6) that has its origin as a solution of a differential equation for forced resonance and describes the shape of spectral lines in spectroscopy. The unilateral rupture propagation with directivity effect compresses the energy released in the forward direction. The directivity-driven $\mu_{\ln(\mathrm{PGV})}$ pattern is analogous to spectral energy peaks, and therefore a Cauchy–Lorentz distribution represents a directivity characterization based on fundamental wave physics. The functional form of this distribution is given as

$$y = \mathrm{I}\frac{\gamma^2}{(x - x_0)^2 + \gamma^2} + C, \qquad (1)$$

in which I, γ, and x_0 are the height, the half-width at half-maximum, and the location parameter, respectively. C is the constant translation term that shifts the level up and down. A small (large) γ indicates that the peak of the distribution is sharp (broad), which implies strong (weak) directivity. Large (or small) values of I represent high (or low) PGV values in forward directivity compared to the backward-directivity region. If there is no directivity, then the pattern of $\mu_{\ln(\mathrm{PGV})}$ will simply be a periodic function due to the S-wave radiation pattern, in which case the Cauchy–Lorentz distribution cannot be used. We estimate the corresponding coefficients using nonlinear optimization of fitting equation (1) to the average $\mu_{\ln(\mathrm{PGV})}$ (Fig. 6).

Analyzing the simulation results for all five rupture models, we find that ground-motion variability is high along the average strike direction (azimuth 0°). Smaller ground-motion variability occurs perpendicular to average strike direction (azimuth ± 90°), but it is high again along the −142.5° direction (Fig. 6). Any potential periodic pattern of $\phi_{\ln(\mathrm{PGV})}$ (due to the S-wave point-source radiation pattern) is distorted due to the complexity of slip and rupture-propagation effects. High $\phi_{\ln(\mathrm{PGV})}$ in the forward direction (azimuth 0°) can be explained by location of fault segments with high slip patches in the forward direction; therefore, high and small values of PGV, and consequently higher $\phi_{\ln(\mathrm{PGV})}$, are found in the corresponding azimuthal bins. Also, unilateral rupture propagation compresses the radiated seismic energy in the forward direction, leading to further increase of PGV values in the bins in the forward direction. However, as the azimuth increases and sites are located farther away from the forward-rupture-propagation direction, the seismic wave energy is more dispersed in time, while the distance from high slip patches increases. In combination, this leads to lower variability of PGV values, and hence $\phi_{\ln(\mathrm{PGV})}$ is low along azimuthal directions ±90°. The azimuth angle −142.5° depicts the backward-rupture-propagation direction with respect to the complex geometry of the fault (see Fig. 3). Hence, the high value of $\phi_{\ln(\mathrm{PGV})}$ along the −142.5° direction is, similarly as for the forward direction, a consequence of the directivity effect. In general, we find that ground-motion variability is high in the forward- and backward-rupture-propagation direction but low in the perpendicular direction. Therefore, the distortion of the periodic pattern of $\phi_{\ln(\mathrm{PGV})}$ is mainly due to directivity. A detailed study on the influence of rupture parameters on azimuthal variation of $\phi_{\ln(\mathrm{PGV})}$ will be presented in the next section.

Comparison of Numerical Simulations with GMPE Estimates

We now compare our numerical results with GMPE estimates to which we apply the directivity correction proposed by Spudich and Chiou (2008) derived for the GMPE by Boore and Atkinson (2008). Because the correction is applicable only to PSA, we compute PSA for natural periods at 5 and 10 s with 5% damping ratio. The GMPE predicts the same value of PSA (or PGV) for a given R_{JB} in all directions (−180° to 180°). The directivity-corrected GMPE accounts for rupture-propagation direction, and consequently PSA values vary spatially even for a fixed R_{JB}.

The directivity correction by Spudich and Chiou (2008) is based on the correction term f_{D}:

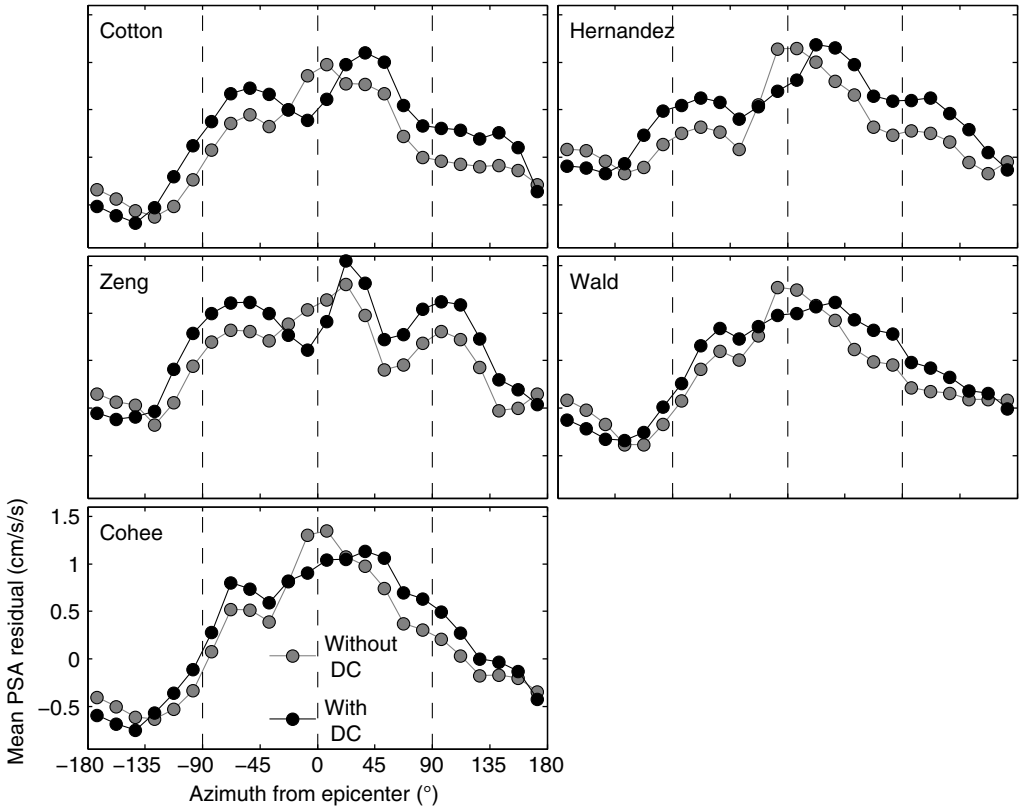

Figure 7. The mean pseudospectral acceleration (PSA) residual (period $T = 10$ s) for the cases with (black) and without (gray) directivity correction (DC) applied to the Boore and Atkinson (2008), as a function of azimuth (bin width=15°); 0° azimuth represents the average strike direction.

$$f_{\mathrm{D}} = f_{\mathrm{r}}(R_{\mathrm{rup}}) f_M(M_{\mathrm{w}})(a + b \times \mathrm{IDP}), \qquad (2)$$

in which

$$f_{\mathrm{r}} = \max\left[0, \left(1 - \frac{\max(0, R_{\mathrm{rup}} - 40)}{30}\right)\right]$$

$$\text{and} \quad f_M = \min\left[1, \frac{\max(0, M_{\mathrm{w}} - 5.6)}{0.4}\right].$$

The factor f_{r} denotes a distance taper that is unity for rupture distances R_{rup} between 0 and 40 km and then tapers linearly to zero at $R_{\mathrm{rup}} \geq 70$ km. f_M is a magnitude taper that is zero for the 0–5.6 earthquake magnitude (M_{w}) range and rises linearly to unity at $M_{\mathrm{w}} \geq 6.0$. Equation (2) includes an isochrone directivity predictor (IDP) that Spudich and Chiou (2008) calculate using the isochrone velocity ratio and the radiation-pattern amplitude at a specific location (Spudich and Frazer, 1984), accounting for complex geometry and rupture-propagation direction.

For computing this directivity correction, the connected segmented geometries (with no overlap between segments) used in the Cotton, Hernandez, and Zeng models are considered as a single-fault rupture from the definition of Spudich and Chiou (2008). The overlapping segments of the Wald and Cohee models are considered as multifault ruptures. Accordingly, each segment of these models has its own hypocenter location, assigned based on the rupture onset time distributions. It should be noted that f_{D} does not account for heterogeneity of slip and rupture speed, both of which strongly affect the radiation pattern and hence directivity effect. Because the directivity correction is zero for $R_{\mathrm{JB}} > 70$ km, we compute f_{D} for 1–71 km R_{JB} range for all five source models at 5 and 10 s periods (Ⓔ Fig. S4).

At each station, we compare residuals $R = \ln(\mathrm{PSA}_{\mathrm{sim}}/\mathrm{PSA}_{\mathrm{GMPE}})$ and $R_{f_{\mathrm{D}}} = \ln(\mathrm{PSA}_{\mathrm{sim}}/\mathrm{PSA}_{\mathrm{GMPE}_{f_{\mathrm{D}}}})$, that is, the residuals with respect to the GMPE estimates without and with directivity correction, respectively. We find only minor differences between R and $R_{f_{\mathrm{D}}}$ for both considered periods (Ⓔ Fig. S5). To further analyze and summarize the differences, we bin the residuals as a function of azimuth (bin width 15°) and calculate the mean for a 10 s period (Fig. 7). The azimuth for each station is computed with respect to the average strike direction (with origin at the epicenter). The mean $R_{f_{\mathrm{D}}}$ residuals are lower than the mean R residuals along the average strike direction (0°) for all five models, indicating that the directivity correction partially captures the directivity effect. However, for the other directions, mean $R_{f_{\mathrm{D}}}$ residuals are higher than mean R residuals. Overall, we find the differences between the mean R and $R_{f_{\mathrm{D}}}$ residuals are insignificant, for all directions. Therefore, our results indicate that

Table 3
Combinations of Heterogeneous and Uniform Rupture Parameters for Cotton Source Model

Model Reference	Model Name	D	Tr	Vr
U_{DTrVr}	m1	U	U	U
$H_D - U_{TrVr}$	m2	H	U	U
$H_{Tr} - U_{DVr}$	m3	U	H	U
$H_{Vr} - U_{DTr}$	m4	U	U	H
$H_{DTr} - U_{Vr}$	m5	H	H	U
$H_{DVr} - U_{Tr}$	m6	H	U	H
$H_{TrVr} - U_D$	m7	U	H	H
Cotton	m8	H	H	H
ptsrc	m9	—	—	—

U, uniform; H, heterogeneous; D, slip; Tr, rise time; Vr, rupture speed; ptsrc, point source.

the directivity correction proposed by Spudich and Chiou (2008) does not fully capture the spatial variations in ground-motion variability. The space–time complexity of the earthquake rupture process is unlikely to be sufficiently described by the IDP term. Directivity effects are averaged by GMPEs because they are derived statistically by combining recordings from many different earthquakes. Likewise, a directivity correction provides an approach to quantify the average, or generalized, directivity behavior, which appears insufficient to capture the directivity signature in simulated ground motions for Landers source models. We also investigated PSA residuals between estimates from observed data (from 10 stations) and the predictions using Boore and Atkinson (2008) for the cases with and without directivity correction. The analysis of observed data confirms our findings from simulations that the Spudich and Chiou (2008) directivity correction has only a small effect and does not capture full directivity signature in ground motions.

Insights on Ground-Motion Variability from Source Heterogeneity

In this section, we investigate ground-motions arising from simplified canonical models to better understand the origins of ground-motion variability and to identify key parameters controlling $\phi_{\ln(PGV)}$.

Canonical Models

We generate seven simplified canonical rupture models based on the Cotton model of the Landers earthquake. Our objective is to analyze how (or if) heterogeneous slip, rise time, and rupture speed affect ground-motion variability. The canonical models, obtained by combinations of heterogeneous and uniform distributions of source parameters, are summarized in Table 3. For example, $H_{DTr} - U_{Vr}$ denotes a rupture model with heterogeneous (H) slip (D) and rise time (Tr) but uniform (U) rupture speed (Vr). Interchangeably with this notation, we will also use the nomenclature m1–m9 (see Table 3). The uniform parameters are obtained

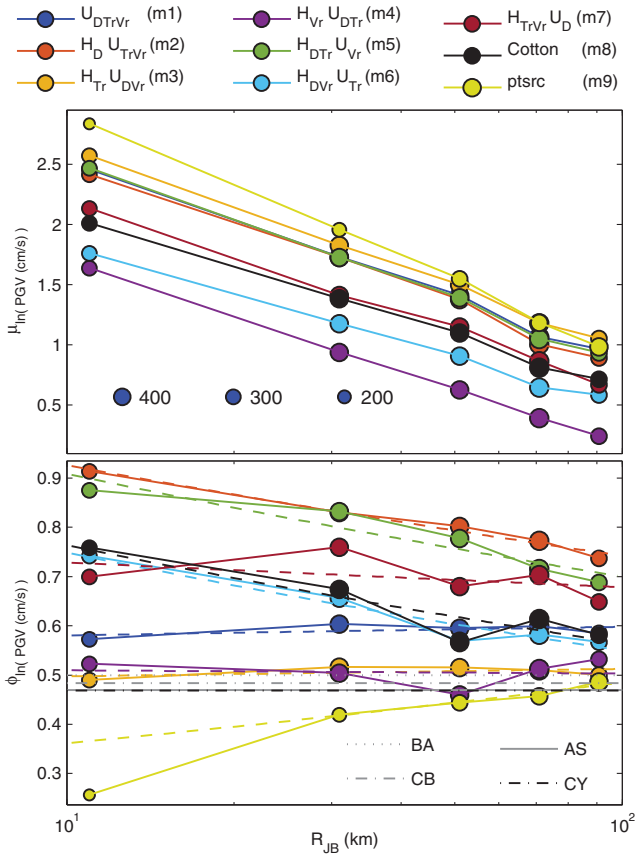

Figure 8. Distance dependence of $\mu_{\ln(PGV)}$ and $\phi_{\ln(PGV)}$ (bin width 20 km) for seven canonical source models (m1–m7), Cotton's model (m8), and point source (m9) (see Table 3 and text for details). The dashed line represents the power-law fit to the corresponding $\phi_{\ln(PGV)}$ values. The marker size represents the number of stations in each bin. Abbreviations are as follows: BA, Boore and Atkinson (2008); CB, Campbell and Bozorgnia (2008); AS, Abrahamson and Silva (2008); CY, Chiou and Youngs (2008); ptsrc, point source.

by computing the spatial average of the corresponding heterogeneous source quantity, resulting in mean values of slip, rise time, and rupture speed of 241.46 cm, 3.18 s, and 2.83 km/s, respectively. Fault geometry and source time function remain unchanged. Furthermore, we consider a point source with the same seismic moment of the Cotton model, using a Brune source time function with rise time identical to the total rupture time of the Cotton model. Including the original Cotton model, we thus compare ground motions for nine canonical models: eight finite-fault models and one point-source model (Table 3). We use the SORD code for seismic-wavefield simulations, applying the station configurations as before (Fig. 3) and the 1D Earth model of the Cotton model.

Distance Dependence

Figure 8 compares the distance dependence of $\mu_{\ln(PGV)}$ and $\phi_{\ln(PGV)}$ of the seven canonical models with those for the

Table 4
Parameters α and k of the Power Law (αR_{JB}^{k}) Obtained from Least-Squares Fitting to the Distance Dependence of $\phi_{ln(PGV)}$ for Nine Sources

Model Reference*	Model Name	α	k
U_{DTrVr}	m1	0.56	0.01
$H_D - U_{TrVr}$	m2	1.16	−0.10
$H_{Tr} - U_{DVr}$	m3	0.48	0.01
$H_{Vr} - U_{DTr}$	m4	0.52	−0.01
$H_{DTr} - U_{Vr}$	m5	1.18	−0.11
$H_{DVr} - U_{Tr}$	m6	1.02	−0.13
$H_{TrVr} - U_D$	m7	0.78	−0.03
Cotton	m8	1.03	−0.13
ptsrc	m9	0.27	0.13

*U, uniform; H, heterogeneous; D, slip; Tr, rise time; Vr, rupture speed; ptsrc, point source.

Cotton model and the point source. We fit the power law, $\phi_{ln(PGV)} = \alpha R_{JB}^{k}$, and obtain the values for the parameters α and k by least-squares fitting (see Table 4).

Figure 8 indicates that slip heterogeneity largely controls the power-law decay of $\phi_{ln(PGV)}$. All three models with heterogeneous slip (i.e., $H_D - U_{TrVr}$, $H_{DTr} - U_{Vr}$, and $H_{DVr} - U_{Tr}$) yield k-values in the −0.13 to −0.10 range, consistent with the original Cotton model for which $k = -0.13$. All other canonical models with uniform slip yield significantly lower k-values in the −0.03 to 0.01 range, that is, k is so small that the resulting $\phi_{ln(PGV)}$ is almost constant.

Figure 8 also suggests that the effects of heterogeneity in rise time (Tr) and rupture velocity (Vr) on $\phi_{ln(PGV)}$ depend on the heterogeneity of slip (D). If slip is heterogeneous, then neither heterogeneous nor uniform rise time cause sizable effects on $\phi_{ln(PGV)}$, (compare solutions m5 with m2 or m8 with m6). However, if slip is uniform, heterogeneous Tr seems to be responsible for lower $\phi_{ln(PGV)}$ (compare solutions m3 with m1). Similarly, if slip is uniform, heterogeneous Vr seems to be responsible for lower $\phi_{ln(PGV)}$ (compare solutions m4 with m1). However, if both Tr and Vr are heterogeneous and slip is uniform, higher $\phi_{ln(PGV)}$ is found compared to the cases of only Tr (or Vr) being heterogeneous (compare solutions m7 with m3 or m7 with m4). This suggests that there is a trade-off between Tr and Vr, which is also supported by similar $\phi_{ln(PGV)}$ values for $H_{Tr} - U_{DVr}$ (m3) and $H_{Vr} - U_{DTr}$ (m4). $\phi_{ln(PGV)}$ computed from simplified models m3 and m4 is close to $\phi_{ln(PGV)}$ estimates for the four GMPEs we use (see Fig. 8 for details).

Next, we analyze $\phi_{ln(PGV)}$ for the point-source model. Because of a small number of stations (only 86) for the distance bin $R_{JB} = 11$ km, we do not consider it statistically robust and excluded it from power-law fitting. Ground-motion variability of a point source is constant with distance as a consequence of fixed ratio of P- and S-wave amplitudes (because both decay with 1/r). Our results, however, indicate a slow increase of $\phi_{ln(PGV)}$ with R_{JB}, as a result of the presence of reflected and refracted body waves, as well as surface waves, generated by the layered-velocity structure. For larger R_{JB}, $\phi_{ln(PGV)}$ is closer to the GMPEs estimates.

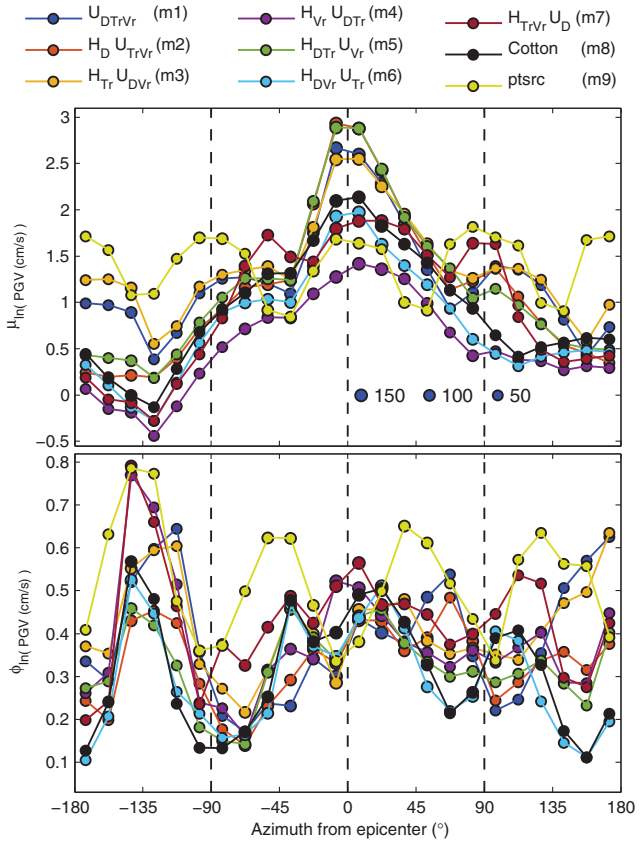

Figure 9. Azimuthal dependence of $\mu_{ln(PGV)}$ and $\phi_{ln(PGV)}$ (bin width 15°) for seven canonical source models (m1–m7), Cotton's model (m8), and point source (m9) (see Table 3 and text for details). The marker size represents the number of stations in each bin; 0° azimuth represents the average strike direction.

From the seven additional finite-fault models, those with heterogeneous slip exhibit a power-law decay with distance, similar to that of the original Cotton model. Uniform-slip models yield a substantially smaller slope k. We also find that slip heterogeneity plays a role in the case of heterogeneous rise time and rupture speed. Our results indicate that slip heterogeneity is the controlling parameter for the power-law decay of ground-motion variability for low frequencies (0–0.5 Hz). However, further analysis is required to precisely quantify effects of slip heterogeneity on the power-law decay of ground-motion variability.

Azimuthal Dependence

Next, we analyze the azimuthal dependence of $\phi_{ln(PGV)}$ for the eight simplified rupture models and the original Cotton model (Fig. 9). The distributions of $\mu_{ln(PGV)}$ have a similar shape to the Cauchy–Lorentz function for the finite-fault models, whereas the point source shows the expected $\pi/2$ periodic S-wave radiation pattern. We fit the Cauchy–Lorentz function to the azimuthal distributions of $\mu_{ln(PGV)}$ and estimate its parameters (equation 1; see Table 5 and

Table 5

Parameters I, γ, x_0, and C obtained from Nonlinear Optimization of Fitting the Cauchy–Lorentz Distribution to the Azimuthal Distribution of $\mu_{\ln(PGV)}$ for the Eight Sources

Model Reference*	Model Name	I	γ	x_0	C	RSS†
U_{DTrVr}	m1	1.93	30.43	5.94	0.8	54.17
$H_D - U_{TrVr}$	m2	2.62	50.37	7.79	0.18	28.13
$H_{Tr} - U_{DVr}$	m3	1.66	35.08	8.12	0.94	86.04
$H_{Vr} - U_{DTr}$	m4	1.71	78.24	12.41	−0.32	62.10
$H_{DTr} - U_{Vr}$	m5	2.54	47.86	7.1	0.29	32.37
$H_{DVr} - U_{Tr}$	m6	1.9	58.82	5.69	−0.02	11.23
$H_{TrVr} - U_D$	m7	3.37	149.52	19.45	−1.48	23.26
Cotton	m8	2.07	66.59	6.21	0.0	0.00

*U, uniform; H, heterogeneous; D, slip; Tr, rise time; Vr, rupture speed; ptsrc, point source.

†RSS, residual sum of squares.

Ⓔ Fig. S6). Table 5 lists the corresponding residual sum of squares (RSS) with respect to the fit to the Cotton model. The four parameters for the model with heterogeneous slip and rupture speed ($H_{DVr} - U_{Tr}$) are close to the Cotton model with lowest RSS. On the other hand, the model with uniform slip and rupture speed ($H_{Tr} - U_{DVr}$) has highest RSS, with large deviation from Cotton (Fig. 9 and Ⓔ Fig. S6), indicating that slip and rupture speed control $\mu_{\ln(PGV)}$. The model with uniform slip $H_{TrVr} - U_D$ shows a broad distribution of $\mu_{\ln(PGV)}$, hence the highest γ-value. We also observe that rise time has the smallest effect on the shape of Cauchy–Lorentz function (compare solutions m6 with m8 or m2 with m5). Thus, the combination of slip and rupture speed controls the shape of Cauchy–Lorentz function, with slip being the dominating parameter.

Figure 9 also reveals that $\phi_{\ln(PGV)}$ of m1–m7 show a similar pattern as the Cotton model, whereas $\phi_{\ln(PGV)}$ from the point source is periodic due to S-wave radiation pattern. Table 6 lists the RSS values of $\phi_{\ln(PGV)}$ with respect to the Cotton model, showing that $\phi_{\ln(PGV)}$ from rupture model m6 with heterogeneous slip and rupture speed is closest to Cotton with lowest RSS (Fig. 9 and Table 6). Models m1 and m3 yield a high RSS value, indicating again that heterogeneity of rise time appears least important. The remaining four models (m2, m4, m5, and m7) also show large values of RSS, but heterogeneous slip leads to significantly lower RSS values for m5 compared to m3, for m6 compared to m4, and for m2 compared to m1. Heterogeneous rupture speed leads to significantly lower RSS value for m6 compared to m2, for m7 compared to m3, and for m4 compared to m1. Based on these observations, we conclude that combination of slip and rupture speed controls the azimuthal pattern of $\phi_{\ln(PGV)}$, but at this point it is difficult to assess which of the two is the dominating parameter.

M_w 7.8 ShakeOut Scenario

Here, we test our hypothesis that ground-motion variability due to unilateral ruptures with directivity effect decays as a power law of R_{JB} and that the decay is primarily controlled by slip heterogeneity. We also test the hypothesis that ground-motion variability is high along the rupture-propagation direction, and low along the perpendicular direction for unilateral ruptures. To this end, we perform simulations for the ShakeOut scenario—a hypothetical M_w 7.8 strike-slip earthquake in southern California, with complex fault geometry and heterogeneous rupture process, embedded in a 3D velocity structure.

Table 6

RSS of $\phi_{\ln(PGV)}$ with Respect to Cotton for the Seven Sources

Source Name*	Model Name	RSS†
U_{DTrVr}	m1	1.06
$H_D - U_{TrVr}$	m2	0.38
$H_{Tr} - U_{DVr}$	m3	0.77
$H_{Vr} - U_{DTr}$	m4	0.38
$H_{DTr} - U_{Vr}$	m5	0.16
$H_{DVr} - U_{Tr}$	m6	0.03
$H_{TrVr} - U_D$	m7	0.48

*U, uniform; H, heterogeneous; D, slip; Tr, rise time; Vr, rupture speed; ptsrc, point source.

†RSS, residual sum of squares.

Kinematic Source

The ShakeOut project developed several earthquake scenarios designed to examine physical, social, and economic consequences of a major earthquake in southern California (Jones *et al.*, 2008). Hypothetically, M_w 7.8 earthquakes are constructed by compiling information from trenching, prehistoric earthquakes, instrumental recordings, and theories of earthquake source physics (Jones *et al.*, 2008). The extent of the fault rupture is determined from geological characteristics. The fault length is 305 km, and rupture depth is slightly variable (average fault width is 14.4 km). We consider the case with the hypocenter located near the southern end of the San Andreas fault and for which the rupture propagates towards the north. The kinematic rupture process follows the description of Graves *et al.* (2008), with an average slip of 4.6 m. The slip distribution is a combination of a characterization by Jones *et al.* (2008) for long length scales (>30 km) and the approach of Mai and Beroza (2002) for short length scales. The source time function is a Brune pulse, with rise time proportional to the square root of slip. Independent source time functions in strike and dip directions allow for temporal rake rotations. Figure 10 shows the distribution of slip on the fault with local variations of strike and dip angles.

Computational Model and Parameters

To replicate the ShakeOut simulation, we use the 3D velocity model CVM4 (Kohler *et al.*, 2003) of the Southern California Earthquake Center with truncated S-wavespeed (V_S min $= 620$ m/s; the P-wavespeed is then modified such

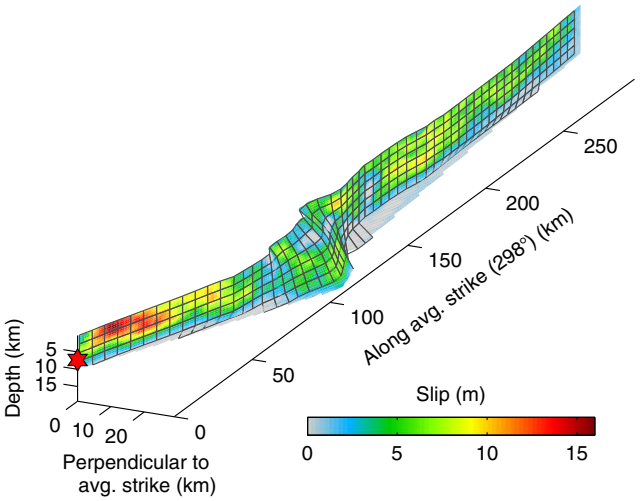

Figure 10. Total slip component (along rake) for a large M_w 7.8 ShakeOut rupture scenario (Graves *et al.*, 2008). The fault has subtle geometric complexities with variations in strike directions and dip angles. The red star denotes the hypocenter. Slip is given in meters.

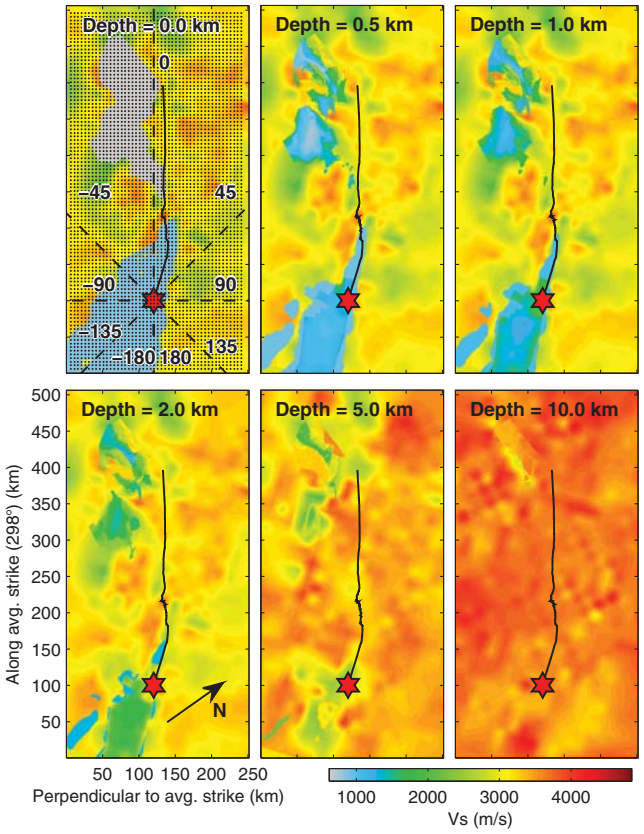

Figure 11. *S*-wavespeed extracted from the community velocity model (Southern California Earthquake Center, CVM4; Kohler *et al.*, 2003) at different depth levels for computing the seismic wavefield for the ShakeOut rupture scenario shown in Figure 10. The black line represents surface projection of the San Andreas fault, the red star marks the epicenter position, and black arrow depicts the north direction. Black dots are the receiver positions. The dashed black lines show the azimuthal directions with respect to the epicenter (chosen as the origin in a Cartesian reference frame).

that local V_P/V_S ratio is conserved). Figure 11 shows horizontal slices of V_S at various depths. To examine the near-field ground-motion variability, we consider a set of 4700 receivers, at a spacing of 5 km (Fig. 11). Our targeted simulation frequency is 0.8 Hz, resulting in a grid size of 50 m and a computational time step $dt = 0.0033$ s. The simulated waveforms are band-pass filtered in the 0.05–0.8 Hz frequency range using a second-order Butterworth filter.

Distance Dependence

We compute PGV from synthetic seismograms at the grid of receivers. PGV values are binned with respect to R_{JB} using bin width of 15 km, applying the same criteria as for the Landers case. We calculate the mean ($\mu_{\ln(PGV)}$) and the associated standard deviation ($\phi_{\ln(PGV)}$) considering a log-normal distribution (Fig. 12). As expected, $\mu_{\ln(PGV)}$ decreases with increasing distance due to geometrical spreading (note that in this case we do not apply Futterman filter). Fitting a power law to $\phi_{\ln(PGV)}$, we obtain $\alpha = 0.94$ and $k = -0.13$. Both parameters, but k in particular, are close to those obtained from average $\phi_{\ln(PGV)}$ of the Landers simulations ($\alpha = 1.11$, $k = -0.14$). Local deviations from the power law are much larger compared to the power-law fit for Landers, in particular for the bin at $R_{JB} \sim 25$ km. We attribute this to effects of 3D velocity structure. We observe that ground-motion variability is much larger in the near-source distances (<25 km) compared to the $\phi_{\ln(PGV)}$ associated with standard GMPEs, but it decreases towards the GMPE-predicted values at larger distance. This is consistent with our results for the Landers earthquake. The ShakeOut rupture is unilateral with very strong directivity effect, which we identified above as the primary reason for the power-law decay of the variability. Thus, our physical and statistical understanding based on Landers simulations is supported by the results for ShakeOut scenario for distance dependence of ground-motion variability.

Azimuthal Dependence

To analyze the azimuthal dependence of ground motion for the ShakeOut scenario, we calculate azimuth with respect to the average strike direction and the epicenter (Fig. 11), and define azimuth-dependent PGV bins of 15° width to compute $\mu_{\ln(PGV)}$ and $\phi_{\ln(PGV)}$ (Fig. 13). Because of strong directivity, $\mu_{\ln(PGV)}$ is highest in the forward-directivity region (azimuth 0°) and lowest in the backward-directivity region (azimuth ± 180°). We find that $\mu_{\ln(PGV)}$ for the ShakeOut simulation is well approximated by the Cauchy–Lorentz function (Fig. 13), consistent with our observations from Landers simulations. The parameters ($I = 2.78$, $\gamma = 40.73$, $x_0 = 7.08$, and $C = 0.94$) are in agreement with the values we found for the Landers simulations ($I = 2.02$, $\gamma = 56.13$, $x_0 = 6.00$,

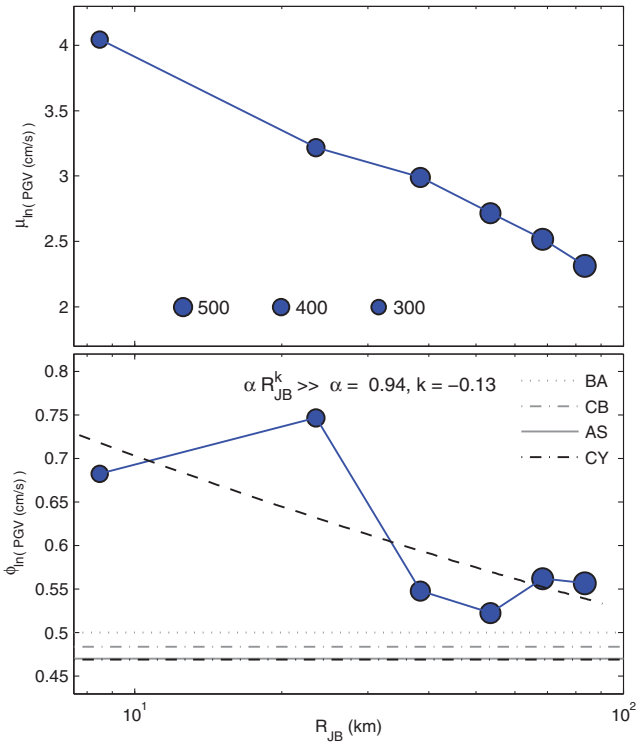

Figure 12. Distance dependence of $\mu_{\ln(PGV)}$ and $\phi_{\ln(PGV)}$ for the ShakeOut scenario simulation (bin width = 15 km). The marker size represents the number of stations in each bin. $\phi_{\ln(PGV)}$ decreases as a power law (αR^k_{JB}) with increasing distance. The dashed black line represents power-law fit to the corresponding $\phi_{\ln(PGV)}$ values. Abbreviations are as in Figure 5.

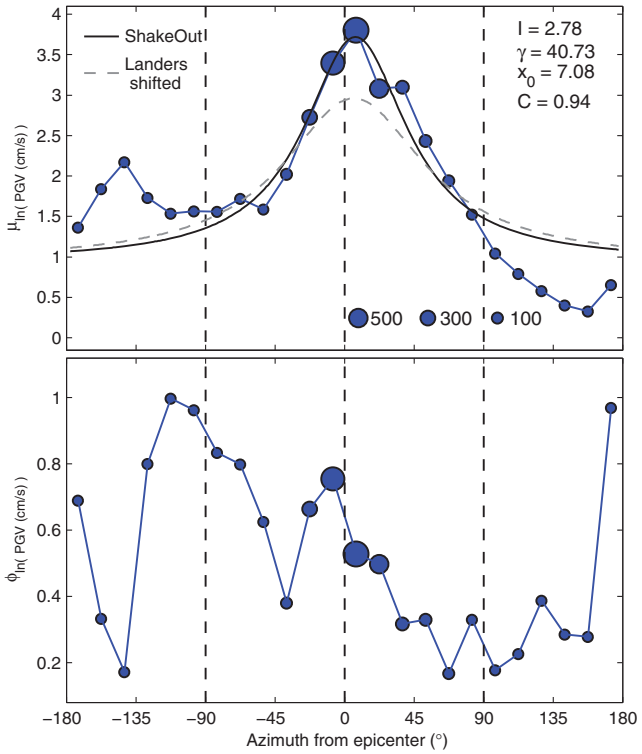

Figure 13. Azimuthal dependence of $\mu_{\ln(PGV)}$ and $\phi_{\ln(PGV)}$ for the ShakeOut scenario simulation (bin width = 15°). The marker size represents the number of stations in each bin. The coefficients I, γ, x_0, and C of the Lorentz function are obtained from nonlinear optimization for $\mu_{\ln(PGV)}$, and the black line depicts the corresponding fit. An additional Lorentz function (dashed gray line) based on parameters estimated from Landers simulations with parameter C equal to ShakeOut is also plotted to facilitate the comparison; 0° azimuth represents the average strike direction.

and $C = 0.45$). For visual comparison, we plot the Cauchy–Lorentz function for the Landers simulations, shifted such that parameter C is equal to that of the ShakeOut scenario (see Fig. 13).

Ground-motion variability is high along the average strike direction (azimuth 0°) and along the backward-rupture-propagation direction (azimuth ± 180°). Interestingly, $\phi_{\ln(PGV)}$ is low along the azimuth +90° but high along −90° (Fig. 13). These findings are generally consistent with our result for the Landers simulations, whereby the high $\phi_{\ln(PGV)}$ along the −90° direction is attributed to 3D velocity heterogeneity and basin effects (Fig. 11).

Overall, the ShakeOut simulation confirms that $\mu_{\ln(PGV)}$ follows a Cauchy–Lorentz function and that $\phi_{\ln(PGV)}$ is high in the rupture-propagation direction but low in the perpendicular direction. Though $\phi_{\ln(PGV)}$ is modulated by 3D heterogeneous Earth structure, these results are consistent with our findings for Landers. Consequently, the ShakeOut results corroborate our previously obtained statistical analysis and physical understanding from Landers simulations on azimuthal dependence of ground-motion variability.

Discussion

Based on our analysis of ground-motion simulations for the 1992 M_w 7.3 Landers earthquake and a hypothetical M_w 7.8 ShakeOut scenario, we find that ground-motion variability due to unilateral ruptures obeys a power-law decrease with distance. Our results indicate that in the low-frequency range, this effect is mainly controlled by slip heterogeneity. We measure similar values for the power-law decay for the Landers ($\alpha = 1.11$, $k = -0.14$) and ShakeOut ($\alpha = 0.94$, $k = -0.13$) events, indicating that the parameters may be relatively stable for different events.

We also find that $\phi_{\ln(PGV)}$ in the very near field ($R_{JB} < 20$ km) is significantly higher than commonly reported in published GMPEs. Our estimates of the intraevent $\phi_{\ln(PGV)}$ for $R_{JB} = 11$ km ($\phi_{\ln(PGV)} \sim 0.6$–1.0) are consistent with those of Imtiaz *et al.* (2015) for unilateral ruptures ($\phi_{\ln(PGV)} \sim 0.5$–1.0). Imtiaz *et al.* (2015) also found distance dependence of $\phi_{\ln(PGV)}$, which they interpreted to be a consequence of the directivity effect. In our study, we develop a quantitative understanding of the distance decay of $\phi_{\ln(PGV)}$ from a statistical point of view (by fitting a functional form) as well as a physical point of view (by analyzing effect of rupture parameters). In our simulations, the relatively high value of $\phi_{\ln(PGV)}$ for $R_{JB} < 20$ km is a consequence of heterogeneous fault slip (as shown in Fig. 8). The influence of heterogeneity of rupture speed and/or rise time is of smaller

importance. We further expect that other factors, such as fault roughness, seismic scattering, or plastic deformation, may also affect the behavior of $\phi_{\ln(\mathrm{PGV})}$ in near field. Fault roughness causes local stress perturbations, leading to localized accelerations and decelerations of the rupture front (Madariaga, 1977), and promotes self-healing pulses (Shi and Day, 2013), leading to increased high-frequency radiation that affects near-field ground motion. Small-scale heterogeneities in Earth structure produce significant high-frequency seismic-wave scattering (Imperatori and Mai, 2013), which results in an apparent isotropic, instead of four-lobed, *S*-wave radiation pattern (Takemura *et al.*, 2009). Inclusion of plastic deformation in rupture dynamics leads to slip-rate saturation and a shift of the corner-frequency towards lower frequencies compared with the elastic case (Andrews, 2005; Shi and Day, 2013). We conjecture that fault roughness and seismic scattering increase near-field ground-motion variability, whereas plasticity may lead to decreased $\phi_{\ln(\mathrm{PGV})}$.

In the far field ($R_{\mathrm{JB}} \sim 100$ km), the $\phi_{\ln(\mathrm{PGV})}$ values estimated from simulations converge to the values of $\phi_{\ln(\mathrm{PGV})}$ given in standard GMPEs. The higher near-field ground-motion variability inferred from simulations may have significant impact on seismic-hazard estimation because the annual frequency of exceedance is highly sensitive to the $\phi_{\ln(\mathrm{PGV})}$, particularly for long return periods (Bommer and Abrahamson, 2006). Our results suggest that PGV values estimated using standard GMPEs with constant $\phi_{\ln(\mathrm{PGV})}$ may be underestimated in the very near field in the case of unilateral and directive ruptures.

Our analyses for the 1992 Landers earthquake and ShakeOut scenario simulations show that intraevent ground-motion variability for unilateral directive ruptures is high in both the forward- and backward-directivity direction but low in the direction perpendicular to rupture propagation. In addition, we observe that the azimuthal dependency of $\phi_{\ln(\mathrm{PGV})}$ is controlled by both rupture speed and slip, but slip heterogeneity seems to be the dominating parameter. Ripperger *et al.* (2008) found that the interevent ground-motion variability is strongest in the backward-directivity region, but they have not analyzed the intraevent ground-motion variability. However, it appears that both the intraevent and interevent ground-motion variability follow similar patterns. We also observe that $\mu_{\ln(\mathrm{PGV})}$ can be modeled using a Cauchy–Lorentz distribution, which captures the effects of strong seismic radiation in the forward-rupture-propagation direction due to directivity.

We find that $\phi_{\ln(\mathrm{PGV})}$ is a function of both distance and azimuth for the Landers earthquake and the ShakeOut scenario for relatively low frequencies (up to 0.5 and 0.8 Hz, respectively). However, high frequencies (up to 25 Hz) are important for engineering purposes and seismic-hazard estimation. For high frequencies, the effects of seismic-wave scattering have to be included (e.g., Imperatori and Mai, 2013). These affect ground motions and their variability already at short distances, at which generally source effects are thought to dominate. Further investigations of ground-motion variability, considering scattering and more complex 3D velocity structures as well as multiple-realistic earthquake-rupture realizations, are needed to better understand the effects of scattering on ground-motion variability for low and high frequencies.

Conclusions

Ground-motion variability $\phi_{\ln(\mathrm{PGV})}$ estimated from numerical simulations of the 1992 M_{w} 7.3 Landers earthquake and the M_{w} 7.8 ShakeOut scenario is higher in the near field ($R_{\mathrm{JB}} < 20$ km) compared to standard GMPEs. This significantly affects probabilistic seismic-hazard assessment, especially for long periods and in the presence of faults that are capable of generating large unilateral earthquake with strong directivity. $\phi_{\ln(\mathrm{PGV})}$ decreases with increasing R_{JB} distance from the fault as a power law ($\alpha R_{\mathrm{JB}}^{k}$) and approaches values of $\phi_{\ln(\mathrm{PGV})}$ estimated by GMPEs at large distances ($R_{\mathrm{JB}} \sim 100$ km). High values of $\phi_{\ln(\mathrm{PGV})}$ in near-source distances are caused by a strong directivity effect. Farther away from the fault, the effect of directivity on ground motion diminishes. Consequently, also $\phi_{\ln(\mathrm{PGV})}$ decreases. Our analyses suggest that the power-law decay of $\phi_{\ln(\mathrm{PGV})}$ is mainly controlled by slip heterogeneity. We also show that intraevent ground-motion variability for unilateral ruptures is large in both the forward- and backward-rupture-propagation direction but low in the direction perpendicular to rupture propagation. We find that $\phi_{\ln(\mathrm{PGV})}$ as a function of azimuth is sensitive to slip heterogeneity as well as rupture speed variations, but the effects of the on-fault slip heterogeneity seem to dominate over the influence of rupture speed. We demonstrate that $\mu_{\ln(\mathrm{PGV})}$ as a function of azimuth is well described by a Cauchy–Lorentz distribution, which provides a novel approach to better predict the spatial dependencies of ground-motion variability for engineering purposes.

Data and Resources

The five kinematic rupture models of the 1992 Landers earthquake are obtained from the Earthquake Source Model Database (SRCMOD; Mai and Thingbaijam, 2014) accessible online at http://equake-rc.info/SRCMOD/ (last accessed March 2016). The recorded seismograms of the earthquake were obtained from the Consortium of Organizations for Strong Motion Observation Systems (COSMOS) database accessible at http://cosmos-eq.org/VDC/index.html (last accessed March 2016). The Southern California Earthquake Center community velocity model CVM4 (Kohler *et al.*, 2003) employed for the ShakeOut simulations is accessible at http://scedc.caltech.edu/research-tools/3d-velocity.html (last accessed March 2016). MATLAB scripts were accessed from www.mathworks.com/products/matlab (last accessed May 2016).

Acknowledgments

We thank Rob Graves for providing us with the source model of the ShakeOut scenario and Paul Spudich for sharing with us his MATLAB

scripts to compute the directivity corrections. We thank Fabrice Cotton for his critical review that helped us to improve the manuscript. We also thank Kiran Kumar Thingbaijam for insightful discussions. The research presented in this article is supported by King Abdullah University of Science and Technology (KAUST) in Thuwal, Saudi Arabia. Earthquake rupture and ground-motion simulations have been carried out using the KAUST Supercomputing Laboratory (KSL), and we acknowledge the support of the KSL staff.

References

Abrahamson, N., and W. Silva (2008). Summary of the Abrahamson & Silva NGA ground-motion relations, *Earthq. Spectra* **24,** no. 1, 67–97.

Akkar, S., and J. J. Bommer (2007a). Empirical prediction equations for peak ground velocity derived from strong-motion records from Europe and the Middle East, *Bull. Seismol. Soc. Am.* **97,** no. 2, 511–530.

Akkar, S., and J. J. Bommer (2007b). Prediction of elastic displacement response spectra in Europe and the Middle East, *Earthq. Eng. Struct. Dynam.* **36,** no. 10, 1275–1301.

Anderson, J. G., and J. N. Brune (1999). Probabilistic seismic hazard analysis without the ergodic assumption, *Seismol. Res. Lett.* **70,** no. 1, 19–28.

Andrews, D. J. (2005). Rupture dynamics with energy loss outside the slip zone, *J. Geophys. Res.* **110,** no. B1, doi: 10.1029/2004JB003191.

Atkinson, G. (2013). Empirical evaluation of aleatory and epistemic uncertainty in eastern ground motions, *Seismol. Res. Lett.* **84,** no. 1, 130–138.

Bindi, D., M. Massa, L. Luzi, G. Ameri, F. Pacor, R. Puglia, and P. Augliera (2014). Pan-European ground-motion prediction equations for the average horizontal component of PGA, PGV, and 5%-damped PSA at spectral periods up to 3.0 s using the RESORCE dataset, *Bull. Earthq. Eng.* **12,** no. 1, 391–430.

Boatwright, J. (2007). The persistence of directivity in small earthquakes, *Bull. Seismol. Soc. Am.* **97,** no. 6, 1850–1861.

Bommer, J. J., and N. A. Abrahamson (2006). Why do modern probabilistic seismic-hazard analyses often lead to increased hazard estimates? *Bull. Seismol. Soc. Am.* **96,** no. 6, 1967–1977.

Boore, D. M., and G. M. Atkinson (2008). Ground-motion prediction equations for the average horizontal component of PGA, PGV, and 5%-damped PSA at spectral periods between 0.01 s and 10.0 s, *Earthq. Spectra* **24,** no. 1, 99–138.

Boore, D. M., W. B. Joyner, and T. E. Fumal (1997). Equations for estimating horizontal response spectra and peak acceleration from western North American earthquakes: A summary of recent work, *Seismol. Res. Lett.* **68,** no. 1, 128–153.

Boore, D. M., J. P. Stewart, E. Seyhan, and G. M. Atkinson (2014). NGA-West2 equations for predicting PGA, PGV, and 5% damped PSA for shallow crustal earthquakes, *Earthq. Spectra* **30,** no. 3, 1057–1085.

Boore, D. M., J. Watson-Lamprey, and N. A. Abrahamson (2006). Orientation-independent measures of ground motion, *Bull. Seismol. Soc. Am.* **96,** no. 4A, 1502–1511.

Campbell, K. W., and Y. Bozorgnia (2008). NGA ground motion model for the geometric mean horizontal component of PGA, PGV, PGD and 5% damped linear elastic response spectra for periods ranging from 0.01 to 10 s, *Earthq. Spectra* **24,** no. 1, 139–171.

Chiou, B. S. J., and R. R. Youngs (2006). Chiou and Youngs PEER-NGA empirical ground motion model for the average horizontal component of peak acceleration and pseudo-spectral acceleration for spectral periods of 0.01 to 10 seconds, *PEER Report Draft*, Pacfic Earthquake Engineering Research Centre, Berkeley, California.

Chiou, B. S. J., and R. R. Youngs (2008). An NGA model for the average horizontal component of peak ground motion and response spectra, *Earthq. Spectra* **24,** no. 1, 173–215.

Cohee, B. P., and G. C. Beroza (1994). Slip distribution of the 1992 Landers earthquake and its implications for earthquake source mechanics, *Bull. Seismol. Soc. Am.* **84,** no. 3, 692–712.

Cotton, F., and M. Campillo (1995). Frequency domain inversion of strong motions: Application to the 1992 Landers earthquake, *J. Geophys. Res.* **100,** no. B3, 3961–3975.

Dumbser, M., and M. Käser (2006). An arbitrary high-order discontinuous Galerkin method for elastic waves on unstructured meshes: II. The three-dimensional isotropic case, *Geophys. J. Int.* **167,** no. 1, 319–336.

Ely, G. P., S. M. Day, and J. B. Minster (2008). A support-operator method for viscoelastic wave modelling in 3-D heterogeneous media, *Geophys. J. Int.* **172,** no. 1, 331–344.

Graves, R. W., B. T. Aagaard, K. W. Hudnut, L. M. Star, J. P. Stewart, and T. H. Jordan (2008). Broadband simulations for M_w 7.8 southern San Andreas earthquakes: Ground motion sensitivity to rupture speed, *Geophys. Res. Lett.* **35,** no. 22, doi: 10.1029/2008GL035750.

Henry, C., and S. Das (2001). Aftershock zones of large shallow earthquakes: Fault dimensions, aftershock area expansion and scaling relations, *Geophys. J. Int.* **147,** no. 2, 272–293.

Hernandez, B., F. Cotton, and M. Campillo (1999). Contribution of radar interferometry to a two-step inversion of the kinematic process of the 1992 Landers earthquake, *J. Geophys. Res.* **104,** no. B6, 13,083–13,099.

Imperatori, W., and P. M. Mai (2012). Sensitivity of broad-band ground-motion simulations to earthquake source and Earth structure variations: An application to the Messina Straits (Italy), *Geophys. J. Int.* **188,** no. 3, 1103–1116.

Imperatori, W., and P. M. Mai (2013). Broad-band near-field ground motion simulations in 3-dimensional scattering media, *Geophys. J. Int.* **192,** no. 2, 725–744.

Imtiaz, A., M. Causse, E. Chaljub, and F. Cotton (2015). Is ground-motion variability distance dependent? Insight from finite-source rupture simulations, *Bull. Seismol. Soc. Am.* **105,** no. 2A, 950–962.

Jones, L. M., R. Bernknopf, D. Cox, J. Goltz, K. Hudnut, D. Mileti, S. Perry, D. Ponti, K. Porter, M. Reichle, *et al.* (2008). The ShakeOut Scenario, *U.S. Geol. Surv. Open-File Rept. 2008-1150 and California Geol. Surv. Preliminary Report 25*, http://pubs.usgs.gov/of/2008/1150/ (last accessed May 2016).

Kohler, M. D., H. Magistrale, and R. W. Clayton (2003). Mantle heterogeneities and the SCEC reference three-dimensional seismic velocity model version 3, *Bull. Seismol. Soc. Am.* **93,** no. 2, 757–774.

Komatitsch, D., and J. Tromp (1999). Introduction to the spectral element method for three-dimensional seismic wave propagation, *Geophys. J. Int.* **139,** no. 3, 806–822.

Madariaga, R. (1977). High-frequency radiation from crack (stress drop) models of earthquake faulting, *Geophys. J. Int.* **51,** no. 3, 625–651.

Mai, P. M (2009). Ground motion: Complexity and scaling in the near field of earthquake ruptures, in *Encyclopedia of Complexity and Systems Science*, W. H. K. Lee and R. Meyers (Editors), Springer, New York, 4435–4474.

Mai, P. M., and G. C. Beroza (2002). A spatial random field model to characterize complexity in earthquake slip, *J. Geophys. Res.* **107,** no. B11, 2308.

Mai, P. M., and K. K. S. Thingbaijam (2014). SRCMOD: An online database of finite-fault rupture models, *Seismol. Res. Lett.* **85,** no. 6, 1348–1357.

Mai, P. M., W. Imperatori, and K. B. Olsen (2010). Hybrid broadband ground-motion simulations: Combining long-period deterministic synthetics with high-frequency multiple *S*-to-*S* backscattering, *Bull. Seismol. Soc. Am.* **100,** no. 5A, 2124–2142.

Mai, P. M., P. Spudich, and J. Boatwright (2005). Hypocenter locations in finite-source rupture models, *Bull. Seismol. Soc. Am.* **95,** no. 3, 965–980.

McGuire, J. J., L. Zhao, and T. H. Jordan (2002). Predominance of unilateral rupture for a global catalog of large earthquakes, *Bull. Seismol. Soc. Am.* **92,** no. 8, 3309–3317.

Mena, B., and P. M. Mai (2011). Selection and quantification of near-fault velocity pulses owing to source directivity, *Georisk* **5,** no. 1, 25–43.

Ramirez-Guzman, L., R. W. Graves, K. B. Olsen, O. S. Boyd, C. Cramer, S. Hartzell, S. Ni, P. Somerville, R. A. Williams, and J. Zhong (2015).

Ground-motion simulations of 1811–1812 New Madrid earthquakes, central United States, *Bull. Seismol. Soc. Am.* **105,** no. 4, 1961–1988.

Ripperger, J., P. M. Mai, and J. P. Ampuero (2008). Variability of near-field ground motion from dynamic earthquake rupture simulations, *Bull. Seismol. Soc. Am.* **98,** no. 3, 1207–1228.

Rodriguez-Marek, A., G. A. Montalva, F. Cotton, and F. Bonilla (2011). Analysis of single-station standard deviation using the KiK-net data, *Bull. Seismol. Soc. Am.* **101,** no. 3, 1242–1258.

Seekins, L. C., and J. Boatwright (2010). Rupture directivity of moderate earthquakes in northern California, *Bull. Seismol. Soc. Am.* **100,** no. 3, 1107–1119.

Shi, Z., and S. M. Day (2013). Rupture dynamics and ground motion from 3-D rough-fault simulations, *J. Geophys. Res.* **118,** no. 3, 1122–1141.

Somerville, P. G., N. F. Smith, R. W. Graves, and N. A. Abrahamson (1997). Modification of empirical strong ground motion attenuation relations to include the amplitude and duration effects of rupture directivity, *Seismol. Res. Lett.* **68,** no. 1, 199–222.

Spudich, P., and B. S. Chiou (2008). Directivity in NGA earthquake ground motions: Analysis using isochrone theory, *Earthq. Spectra* **24,** no. 1, 279–298.

Spudich, P., and L. N. Frazer (1984). Use of ray theory to calculate high-frequency radiation from earthquake sources having spatially variable rupture velocity and stress drop, *Bull. Seismol. Soc. Am.* **74,** no. 6, 2061–2082.

Strasser, F. O., N. A. Abrahamson, and J. J. Bommer (2009). Sigma: Issues, insights, and challenges, *Seismol. Res. Lett.* **80,** no. 1, 40–56.

Takemura, S., T. Furumura, and T. Saito (2009). Distortion of the apparent *S*-wave radiation pattern in the high-frequency wavefield: Tottori-ken Seibu, Japan, earthquake of 2000, *Geophys. J. Int.* **178,** no. 2, 950–961.

Varela, C. L., A. L. Rosa, and T. J. Ulrych (1993). Modeling of attenuation and dispersion, *Geophysics* **58,** no. 8, 1167–1173.

Wald, D. J., and T. H. Heaton (1994). Spatial and temporal distribution of slip for the 1992 Landers, California, earthquake, *Bull. Seismol. Soc. Am.* **84,** no. 3, 668–691.

Youngs, R. R., N. Abrahamson, F. I. Makdisi, and K. Sadigh (1995). Magnitude-dependent variance of peak ground acceleration, *Bull. Seismol. Soc. Am.* **85,** no. 4, 1161–1176.

Zeng, Y., and J. G. Anderson (2000). Evaluation of numerical procedures for simulating near-fault long-period ground motions using Zeng method, *Pacific Earthquake Engineering Research Center*, available at http://peer.berkeley.edu/ (last accessed May 2016).

King Abdullah University of Science and Technology
Division of Physical Sciences and Engineering
Thuwal 23955-6900
Kingdom of Saudi Arabia
Jagdish.Vyas@kaust.edu.sa

Manuscript received 29 October 2015;
Published Online 21 June 2016